.

Dual-band Reflectarray Antennas Using Integrated Resonant and Non-Resonant Natures of Metallic Waveguide Elements at Millimeter Wave Frequencies

H.-T. Chou[1], N.-N. Wang[2], M. Fang[2], L.-Q. Wang[2], P. Akkaraekthalin[3], and D. Torrungrueng[4]

[1]Graduate Institute of Communication Engineering, National Taiwan University, Taipei 10617, Taiwan.

[2] School of Electronics and Information Eng., Harbin Institute of Technology, Harbin 150001, China.

[3] Department of Electrical and Computer Engineering, Faculty of Engineering, King Mongkut's University of Technology North Bangkok, Bangkok 10800, Thailand.

[4] Research Center of Innovation Digital and Electromagnetic Technology, Department of Teacher Training in Electrical Engineering, Faculty of Technical Education, King Mongkut's University of Technology North Bangkok, Bangkok 10800, Thailand.

Corresponding author: Danai Torrungrueng ()

Key Points:

- This paper proposed to develop configurable composite reflecting elements for dual-band reflectarray antennas with easy fabrication characteristics by using die-casting technology.
- The configurability allows the reflectarray to operate at two frequency bands with separated focusing mechanism, analogous to a simultaneous operation of two overlapped reflector or reflectarrays at these two frequency bands.

Abstract

Pure metallic reflectarray antennas have good power efficiency and low fabrication cost, which were limited to single band operation. A dual-band reflectarray antenna is developed for two directional beams by two feeds. The reflecting elements are metal waveguides, and have novel properties of both resonant and non-resonant modes at the two frequency bands. The low and high frequency bands can be easily separated by the cutoff frequency of waveguide modes. The phase changing mechanisms via ray optics and fundamental waveguide modes, respectively provide simple formulations for elemental structure design of directional beams. Radiation characteristics of the linear and circular polarizations are cross-examined with good performance by full-wave simulations using HFSS, FEKO and CST at 28 and 60 GHz bands for 5G front-haul network applications.

**Plain Language Summary**

A metal reflectarray antenna is presented by using waveguide type elements for dual-band operation. Both linear and circular polarization radiations have been examined for this hybrid reflectarray architecture. This type of hybrid antenna elements has shown great potentials for reflectarray antennas with very high-power efficiency.

## 1 Introduction

Metallic reflectarray antennas have good power efficiency and low fabrication cost to provide high antenna gain for propagation loss compensation in air at millimeter wave (mmW) frequencies (An et al., 2014; Cho et al., 2011; Chou et al., 2015, 2016, 2018a, 2018b; Deng et al., 2016a, 2016b, 2017b; Lee et al., 2015, 2017; Wang et al., 2017; Yi et al., 2014). They are superior than the realizations of using PCB substrates, which are very lossy at mmW frequencies(Bozzi et al., 2004; Rajagopalan et al., 2008). This work is motivated by the need of back- and front-haul networks (Chou et al., 2016, 2018a, 2018b, 2020; Wang et al., 2017) implemented at multiple frequency bands including 28, 38 and 60 GHz of interest for 5G mobile communications (Chou et al., 2016, 2018a, 2018b; Wang et al., 2017).

This paper presents an effective architecture of dual-band metallic reflectarray antennas (Deng et al., 2017b; Wang et al., 2017; Zhao et al., 2017) as illustrated by the scenario in Figure 1, to radiate two directional electromagnetic (EM) beams. The concept was preliminarily initiated in (Wang et al., 2017), and is extensively studied for an easy design procedure, where detailed implementation formulations and procedures are described. Practical examples are shown to exhibit the radiation characteristics and validation. Like other dual-band reflectarrays (Deng et al., 2017a, 2017b; Malfajani et al., 2014; Wang et al., 2017; Zhao et al., 2017) this design has relative flexibility of feed illumination and beam radiation. The illumination can be from either a single dual-band or two single-band feed antennas (Chou et al., 2020; Wang et al., 2017). Moreover, the beam directions at these two frequency bands can be different in general.

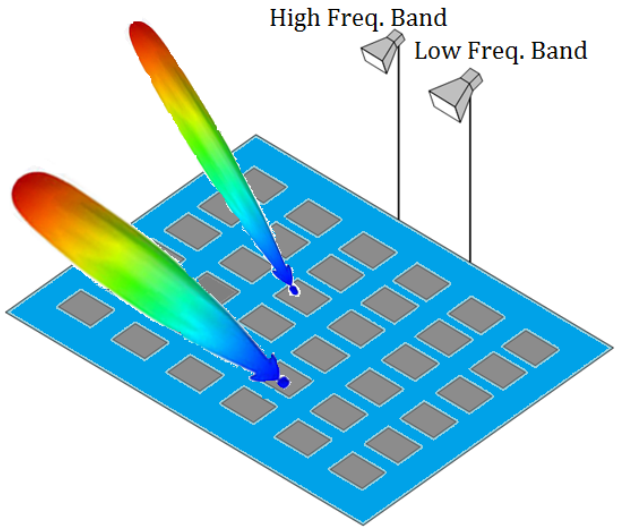


**Figure 1.** Dual-band reflectarray antenna illuminated by two general single-band feeds for two directional beams.

In this new design, the reflecting element is a bottom-terminated straight waveguide with an open-end aperture (Berry et al., 1963). Two operational resonant and non-resonant modes (Chou et al., 2015, 2018b, 2020) of EM scattering are produced by the mechanism of wave propagation in the waveguide at two frequency bands above and below the cutoff frequency of the waveguide's fundamental mode, respectively. Thus, at frequencies far above the cutoff, the element is in the resonant mode (Berry et al., 1963; Chou et al., 2020; Wang et al., 2017), which couples the illuminating fields into the waveguide. The phase delays by reflecting elements to form a directional beam are produced by the wave propagation in the waveguides until it reaches the open-end aperture to radiate in free space. On the other hand, at frequencies below the cutoff, the elements switch to the non-resonant mode (Chou et al., 2015, 2018a; Lee et al., 2015; Wang et al., 2017), and makes the waveguide waves highly evanescent to inactivates in-waveguide phase delays. The wave is directly scattered from the waveguide top aperture (Chou et al., 2015, 2018a; Lee et al., 2015; Wang et al., 2017). The required phases to form directional beams are achieved by the relative heights of elements with respect to a reference plane, whose variation is governed by the geometric optics (GO) ray paths from the feed source to the beam direction via scattering from the reflecting elements.

In comparison to the PCB based resonant reflectarray, the novelty is that it may be very compact in physical profile at mmW frequencies, very different from the old impression of bulky and heavy sizes at low frequencies. Owing to the progress of fabrication technologies, the manufacture is also very accurate at lower cost. It may be fabricated as an integrated metal piece by a simple 3-D printing or die-casting procedure. As pointed out by the previous works of single band

operation (Chou et al., 2015, 2018a), the operational frequencies are relatively broad as exhibited by the natures of GO rays and waveguide modes. It is noted that Chou et al. (2020) embedded the high-frequency (HF) waveguide elements on a parabolic reflector to achieve a dual-band operation. In comparison to the proposed architecture, the concave surface profile of a parabolic reflector not only takes a large space to accomodate, but also produces a blockage to scattered fields for wide-angle beams. On the other hand, the proposed flat dual-band antenna provides higher flexibilty in the directional beamforming.

In practice, the elemental structure is first designed in the non-resonant mode for the low frequency (LF) band. Afterward, from this existing LF structure, the element is etched as a waveguide to produce the resonant mode for the HF band. Thus, the phase delays by the existing LF structures in the non-resonant mode are also accounted in building the required phases in the resonant mode for the HF band. In other words, at the HF band both behaviors of resonant and non-resonant modes are used to produce proper phases. To demonstrate this concept, elements of rectangular cross-section are first designed for linear polarization while circular polarization is implemented by using cross-shape rectangular waveguides. The radiation characteristics are validated by full-wave simulations using HFSS, FEKO and CST (Ansys HFSS, 2013; Dassault Systèmes, 2012; FEKO, 2011) which have been widely validated by measurements on antenna prototypes of similar reflecting element structures. In particular, single-band reflectarrays formed by the non-resonant elements were experimental validated at 12, 38, and 80-105 GHz in Chou et al. (2015), (2018a) and Pozar (1998), respectively. On the other hand, the reflectarray formed by resonant elements was experimentally validated at 80-110 GHz in Balanis (1997). The validations of these reflectarrays at the W-band frequencies well assure the full-simulation validity in this paper to show the radiation characteristics.

The rest of this paper is formatted as follows. Section 2 summarizes basic characteristics of reflecting elements. Section 3 describes the reflectarray composition for the dual band operation. Numerical characteristic investigation of feed illumination over the waveguide elements are presented in Section 4. The reflectarray antenna and its validation by numerical simulations are shown in Section 5. Finally, Section 6 presents conclusions and future developments.

## 2 Characteristics of Elemental Waveguide Structure

### 2.1 Non-Resonant Mode Behaviors

When (cutoff frequency of the waveguide fundamental mode), the waves in the waveguide are evanescent without phase delay. The waveguide behaves as a solid metal pole as illustrated in Figure 2a, where the aperture at is equivalently terminated to scatter all fields from it. The relative phase differences are extracted from the aperture location at .

The excitation amplitude taper to the waveguide elements is determined by the feed's radiation pattern and power divergence along propagation in air. The scattering coefficient by the waveguide is nearly constant, and simply contributes

to a constant phase offset. Thus, the phases of reflecting element mainly vary with respect to the position of the waveguide's open aperture„ as interpreted by geometrical optics (GO) in Chou et al. (2015), (2018b) and Lee et al. (2015), which gives

, (1)

where is the vector wavenumber of the EM scattered field. It is noted that Equation 1 exhibits a linear variation with respect to frequency, and the directions of incident and scattered fields that are oblique to the normal direction of the reflectarray.

2.2 Resonant Mode Behaviors

The waveguide element, configured on a reference plane at in Figure 2b, has an aperture of . It is oriented along the axis with its top aperture and bottom termination at and , respectively to define a depth by . and are the first two waveguide modes by selecting . The cutoff frequency, , of the mode (Almajali et al.,2014; Rahmat-Samii & Lee, 1983) with separates the frequency bands of resonant and non-resonant modes, where is the cutoff wavelength.

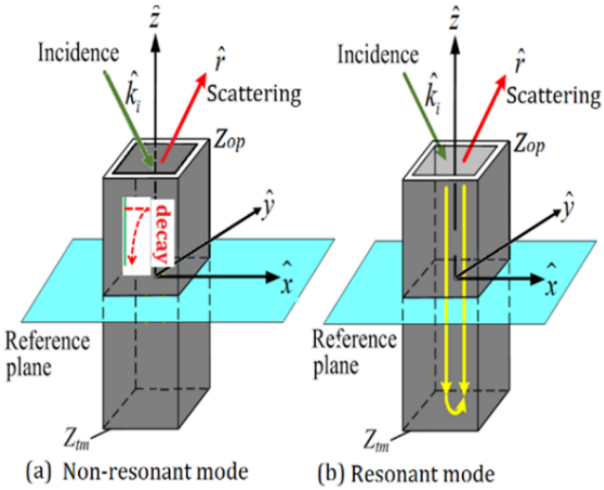


**Figure 2.** Architecture of waveguide reflecting element and the scattering mechanisms for non-resonant and resonant modes in (a) and (b), respectively.

The resonant mode of operation is thus defined at. To assure a reasonable size, it is selected by or with being the free space wavelength, where is a reasonable choice. As shown by the mechanism in Figure 2b, at , the feed radiation illuminating the reflecting element couples into the waveguide, propagates inside, and is reflected from the bottom at to produce a phase delay. The wave re-radiates EM fields into free space from the open-end aperture at .

### 2.2.1 Amplitude Taper Behavior of Illumination

In addition to the feed's radiation pattern effects described in Section 2.1, polarization loss factor (PLF) (Almajali et al.,2014) introduces an extra amplitude weighing for the resonant mode (Chou et al., 2020) as governed by the reaction theorem (Rahmat-Samii & Lee, 1983). In this case, a part of incident wave couples into the waveguide to produce a phase delay while the rest reflects back due to the impedance miss-match by the junction at . Also, the total reflections at the waveguide bottom produce a phase shift. Detailed behaviors are referred to Chou et al. (2018b) and (2020).

Based on the coupling mechanism of resonant mode in Figure 2b, the net reflection coefficients at is approximated by

, (2)

where and are the waveguide wavenumber and impedance, respectively (Rahmat-Samii & Lee, 1983). In Equation 2, is an equivalent impedance of free space to establish an analogous circuit relation to . A good approximation considers the ratio of co-polarized electric and magnetic field components along the waveguide axis direction. It is noted that in the non-resonant mode, the exponential term vanishes to make , as mentioned in Section 2.1. In this case, the illumination energy at the open end will be scattered directly from the open aperture.

### 2.2.2 Phase Variations

The produced phase with respect to the reference plane includes the in-waveguide phase delay in Equation 2, and that by the offset of the waveguide's open aperture. In this case, the scattered field results in a phase variation by

. (3)

Note that is not linear of , which also takes into account of the incident illumination directions that can be oblique to the waveguide opens (Chou et al., 2020). These two separated phase variation mechanisms in Equations 1 and 3 assure a proper design of dual-band reflectarray antenna in the next section. It has been shown in Chou et al. (2020) that full-wave simulation of single waveguide element can be incorporated for phase interpolation of finding . It is performed by determining an effective, , for Equation 2 to match with the simulation result at under the condition of matched phase at by phase offset. It is noted that at and , the phases are 0 and , respectively regardless of the reflection coefficient, . As a result, Equation 3 can be re-formatted as

, (4)

where is effective distance to account for the phase center of waveguide element, and is the constant phase deviation when matching with the full-wave simulation of a single waveguide.

3 Formation of Dual-Band Reflectarray Antennas

The reflecting elements form a dual-band reflectarray antenna at , where and are in the low and high frequency bands, respectively. To assure and being the lowest two modes, it is selected by () and , where is the wavelength at . It is noted that grating lobes will appear when .

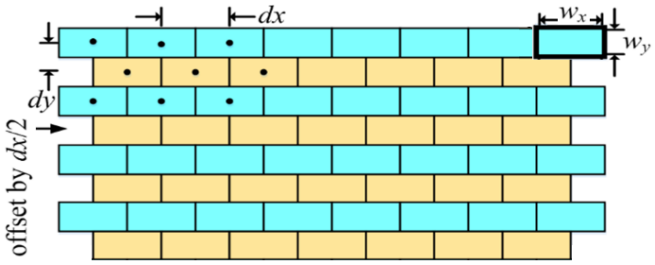


**Figure 3.** Formation of linearly polarized reflectarray with geometric parameters labelled.

The cutoff frequencies of and modes are given by and . For , it can be shown that . It is also noted that , which allows one to define the applicable range of low frequency band, i.e., . Note that a smaller results in a longer waveguide to achieve the required phase variation because make . On the other hand, a large will cause grating lobes when beam deviation is required. To minimize this effect, interleaved arrangement of elements in adjacent rows is performed as illustrated in Figure 3, where and are the periods which are varied to control the phase velociety and amplitude. In this case, the locations of even row elements are shifted by a half period to reduce the projected period on the $x$-axis.

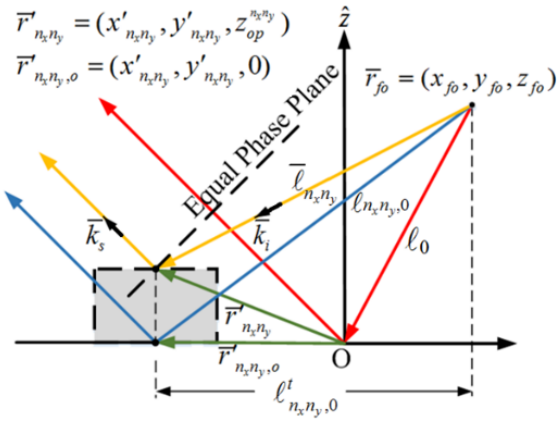


**Figure 4.** Geometrical illustration of reflecting element illuminated by the feed, where the GO rays are shown to demonstrate the phase variation.

In the practical design, the elemental structures are first designed at the low frequency band. Consider the illustration in Figure 4, the height of the element, , is adjusted to create the phases, by using Equation 1 for focusing the beam to the direction, where the subscript " " is used to indicate the low frequency band.

Thus, is determined by enforcing equal-phases for the fields scattered from the reflecting elements along this beam direction. Thus

, (5)

where is the wavelength at . The minimum requirement of appears at

. (6)

The design of high-frequency band elements first employs the locations of waveguide open aperture found in Equation 5, and scales the phases to the higher frequency band by a ratio of . These phases are stored, and are afterward used as the basic phases to design the depths of waveguide to form the directional beam in by using Equation 3, where the subscript "$h$" is used to indicate the high frequency band. In this case, the required phase produced by the reflecting element is given by

. (7)

The waveguide depth is found from solving Equation 2 by equaling Equations 7 and 3, where interpolation can be applied to find the depth from full-wave simulations.

4 Numerical Radiation Characteristic Investigation of Reflecting Element

The characteristics of elemental structure are validated by full-wave simulations using HFSS (Ansys HFSS, 2013). It is noted that the characteristics of non-resonant mode have been previously validated in Chou et al. (2016). We thus focus our attention to the resonant mode at 60 GHz. The center frequencies in the low and high frequency bands are selected by 28 and 60 GHz which result in free space wavelengths byand, respectively. The dimensions of waveguide cross-section are to result in a cutoff frequency by 50 GHz. In this case, is used to make .

## Amplitude Tapering due to the Coupling Effect

In the examination of amplitude tapering, full-wave simulations consider a set of two waveguide antennas facing to each other in their far-field zone, where the waveguide of reflecting element serves as the receiving (RX) waveguide. In this examination, the transmitting (TX) waveguide radiates same power by a unit power weighting on its wave port to illuminate the RX waveguide. As illustrated by the inset in Figure 5, the TX waveguide rotates along various angular directions on the $x$-$z$ and y-z planes in the spherical coordinate system of . The separate distance, , between two waveguides is fixed to remove the power divergence factor and pattern taper of the feed's radiation in the reflectarray applications. It allows one to examine the effect of polarization loss factor.

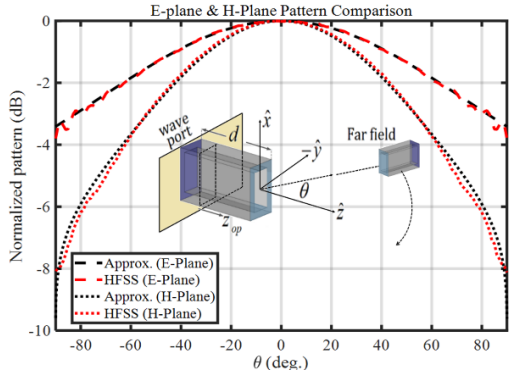


(a) Amplitude taper

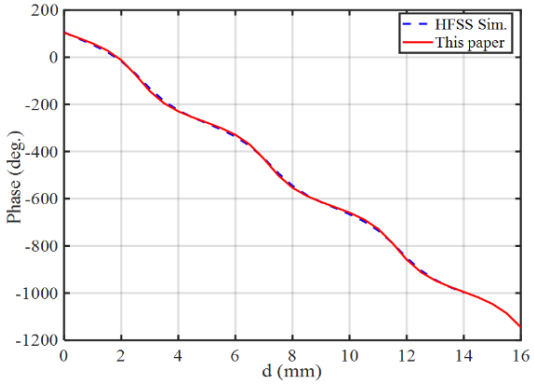


(b) Phase

**Figure 5.** Normalized amplitude tapers and phase delays at 60 GHz.

Also, the termination of the receiving (RX) waveguide is removed to establish a wave port to examine the field coupled into the waveguide. As a result, the power amplitude tapering can be extracted from the insertion loss„ between the wave ports of the two waveguides. In this case, the depth of waveguide, . The results with respect to the incident angles of TX waveguide radiation's illumination on the two principal planes, and 90 degrees are shown in Figure 5a at 60 GHz, where the patterns are normalized to demonstrate the taper behaviors. The approximated results in Figure 5a are obtained by using the solution in Chou et al. (2020). The amplitude on the H-plane has a higher taper than that on the E-plane.

On the other hand, the coupled power into the RX waveguide is very weak at 28 GHz. Numerical simulations show the magnitudes of are smaller than -70dB and are ignorable when the power effects are removed. This insignificant power entry assures the validity of the phase adjustable mechanism of EM scattered fields by the heights of the non-resonant waveguides at 28 GHz.

## Phase Variation Characteristics

The wave port of the RX waveguide is terminated with a metal plate to extract the phase of reflection coefficient, by building a Floquet port on the TX waveguide to compute , where normal incidence is considered. One fixes the location of waveguide open aperture atto examine the effect of waveguide depth, $d$, in phase production. As shown by the results at 60 GHz in Figure 5b, the phase variation exhibits a monotonic behavior with nearly linear but periodic variation. The period is about 4.5 mm, equivalently a half waveguide wavelength at 60 GHz. It is seen that the agreement between the proposed formula in Equation 3 and full-wave simulation is found to be very good. This phase behavior can be used to determine the depths of waveguides at the resonant mode for reflectarray applications. Noted that for easy implementation, one may also use linear interpolation based the full-wave simulated phase variations.

1. Implementation and Radiation Characteristics of Dual-Band Reflectarray by Full-Wave Simulation

5.1 Linear Polarization Radiation Case

The LF and HF feeds were separately implemented at two different locations, as shown in Figure 6. The reflectarray was formed by elements on the x-y plane to make an aperture size by (roughly at 28 GHz). The periods are 4 and 2.5 mm along x- and y-dimensions, respectively. The reflectarray is offset by mm to avoid feed blockage, and has a focal length of (86 mm) with an $F/D$ ratio by 0.67. FEKO was used for simulation.

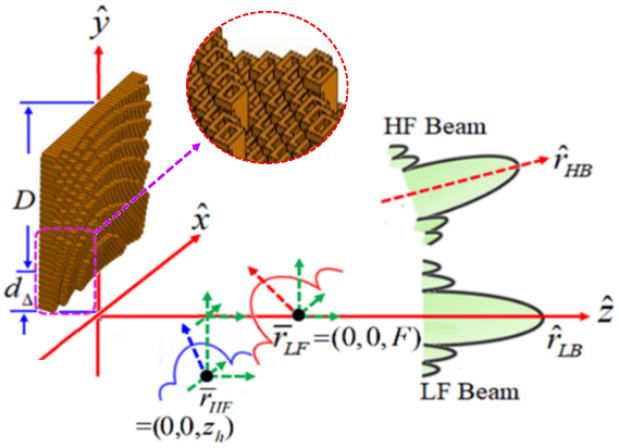


**Figure 6.** Numerical model of the reflectarray and feed placements, where two feeds at 60 and 28 GHz are separately implemented to produce two beams.

For simplification, the feeds at both frequencies were modeled by same cosine tapers to radiate -polarized electrical field by

, (8)

where is the position in the feed's spherical coordinate system (Wang et al., 2018). Their -10 dB beamwidths are 70° to make . The feeds were placed at and for the 28 and 60 GHz bands, respectively, whose main beams pointed to the center of the reflectarray and generate specular reflections by 41° and 62°. Note that the feed position at results in a defocused beam deviated to the 23.8° direction if a conventional reflector is employed.

In the first case, the main beams at both frequencies were specified to the aperture boresight,. Thus, the reflectarray resembles two overlapped parabolic surfaces with different focal lengths to radiate the directional beams. As shown by the results in Figures 7a and 7b for the cases at 28 and 60 GHz, respectively, where the gains are 28.54 and 32.31 dBi at the boresight direction, indicating focusing radiations. It is noted that the reflectarray has a small effective aperture at 60 GHz due to a small illumination area by the feed on the reflectarray because the feed at 60 GHz is closer to the array aperture. In addition, feed image lobes (Almajali et al., 2014) were also observed in these two cases to result in high SLLs in the angular regions near 40 and 62 degrees, respectively as expected in the specular reflection directions. It causes the higher SLLs at 28 GHz. The X-Pol levels on the E-plane are very low in both cases due to the uses of rectangular waveguide elements. The feed image lobes are not apparent at 60 GHz. The SLLs on the H-planes are also very low at both frequencies. The high SLLs at 60 GHz within +/-30° arisen from the metal waveguide frame elements which are non-resonant and are phased by the GO mechanisms as employed at 28GHz. The metal frame scattering effects are produced by the consideration of fabrication limitation. The methods to reduce SLLs include thinning the waveguide wall thicknesses, and reducing operational frequencies, or height discontinuities of the metal frames.

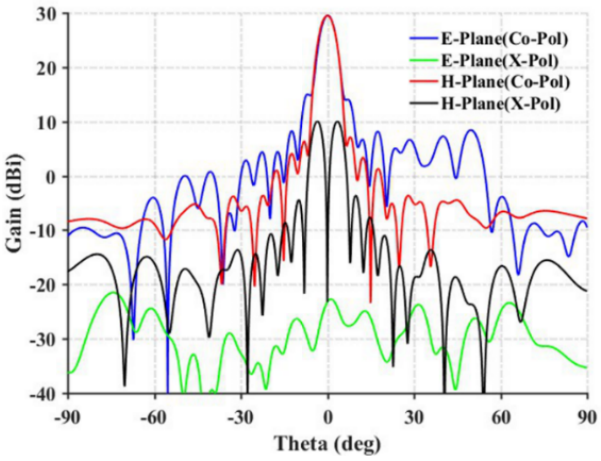


(a) at 28 GHz

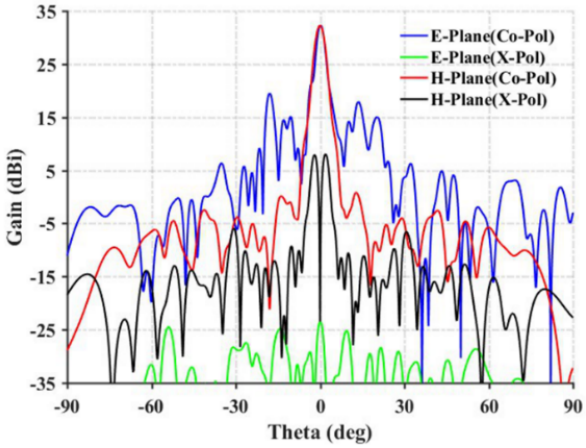


(b) at 60 GHz

**Figure 7.** Radiations of the dual-band reflectarray antenna on the two principal planes at 28 and 60 GHz in (a) and (b), respectively, where beams are in the antenna's boresight directions.

To validate this explanation, the main beam at 28 GHz was tilted toward the specular direction of the feed's illumination at 40° while retaining the beam direction to the antenna boresight at 60 GHz. The radiation patterns are shown in Figures 8a and 8b, respectively, where in Figure 8a only the E-plane patterns are shown due to the reason that the H-plane patterns are now along the sidelobe region. At 28 GHz, it is seen that the gain is 28.41dBi, and is similar to the case of boresight radiation in Figure 7a with a very slight drop (1 dB) due to elemental pattern effect. The SLLs are lower, and nearly monotonically decrease, where the feed image lobes are now embedded in the main beam. The XPL on this E-plane is also very low as expected, where the XPL on the H-plane has also been significantly improved. On the other hand, the E-plane patterns in Figure 8b at 60 GHz have been clearly improved. The gain is similar by 32.58 dBi. The SLLs near the main beam have been significantly reduced in comparison to Figure 7b.

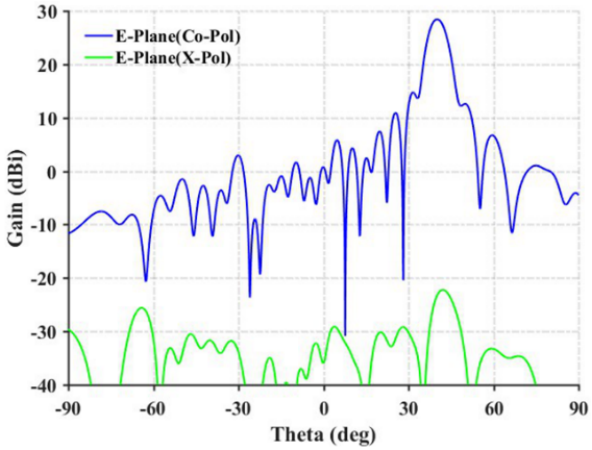


(a) 28 GHz

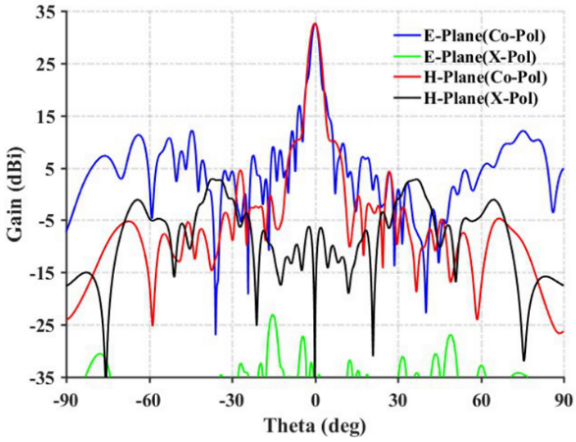


(b) 60 GHz

**Figure 8.** Simulated vertical E-plane patterns at 28 and 60 GHz in (a) and (b), respectively when the beam at 28 GHz is specified to the specular direction.

Finally, the gain variations with respect to frequencies at these two frequency bands are shown in Figure 9. It is seen that the gains of the boresight beam in the 28 GHz band has a more rapid variation to result in narrower bandwidth. The gains of the tilted beam in the specular direction are smaller near 28 GHz due to the elemental pattern effect. They however increase for the frequencies out of this region. At the higher frequencies, it is due to the increase of effective aperture with frequency. At lower frequencies, the phase variations are smoother to retain a better focus than the case of boresight radiation. The gain variation at 60 GHz in Figure 9 is associated with the case of Figure 8b. The variation behavior is similar to the case at 28 GHz for the boresight radiation except with a higher decay speed at higher frequencies. It is seen that to achieve a

broad bandwidth of gain variation, beam radiation along the specular direction is desired. In this case, the 1 dB gain drop bandwidth is better than 13.2% while it is 8.2% for broadside radiation. In this case, the bandwidth is 2.67% for broadside radiation at 60 GHz. The aperture efficiencies are 41 and 21% for broadside radiations at 28 and 60 GHz, respectively. The aperture efficiency at 60 GHz is much smaller because it was placed very close to the aperture that does not fully use the aperture. The aperture efficiencies can be improved by moving the positions of the feed to an outer location. It is thus desired to design dual-band feeds or place two single-band feeds as close as possible to produce close specular directions.

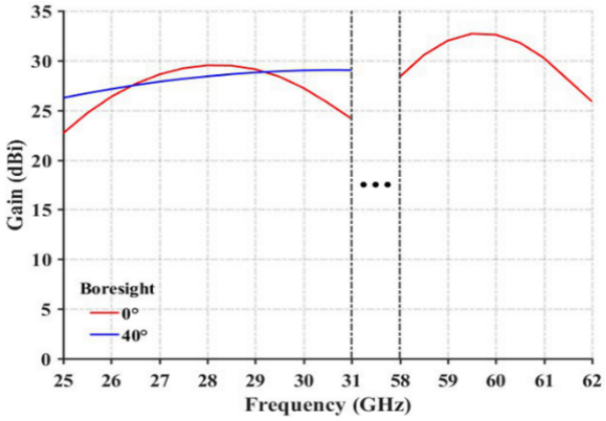


**Figure 9.** Gain variations with respect to frequencies of the dual-band reflectarray antennas at 28 and 60 GHz.

## Circular Polarization Radiation Case

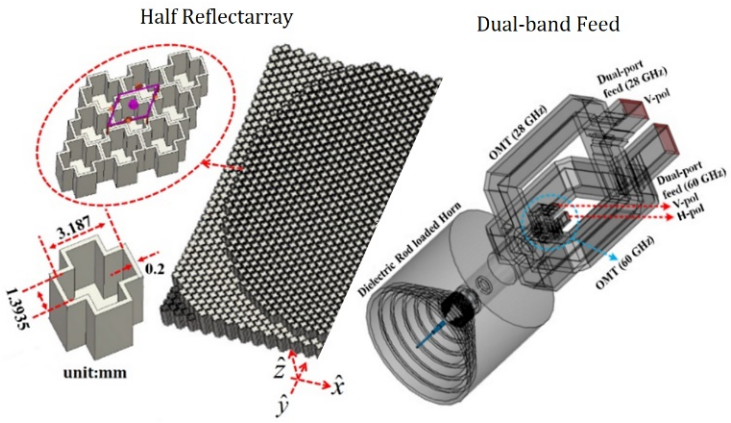


**Figure 10.** Reflectarray with cross-shape rectangular waveguide elements for dual-band circular polarized radiations, where the feed is also shown.

The reflectarray architecture of circular polarization was composed by cross-shaped rectangular waveguides to make aperture size of $mm^2$, slightly larger than the cases in Section 5.1 due to the arrangement of reflecting elements. As illustrated in Figure 10, the adjacent rows are interleaved by a half period to avoid grating lobes and increase aperture efficiency. The elements have dimensions of inner rectangular walls by $mm^2$ with a 0.2 mm wall thickness (the actual wall thickness between adjacent elements is 0.4 mm), which are slightly longer but narrower than the cases in Section 5.1. The thickness of walls is also thinner. This cross-shaped rectangular waveguide has a cutoff frequency at 55 GHz by CST simulations (Dassault Systèmes, 2012), where the phase variations were obtained from interpolation by following the above described procedure in Sections 2-4. The reflection coefficients by the waveguide at 60 GHz is better than -42 dB. The reflectarray is offset by 13.74 mm from the feed's vertical position. The F/D was increased from 0.67 in part A to be roughly 1 in this case, which reduces the discontinuities of elemental height difference for a better radiation patterns at 60 GHz.

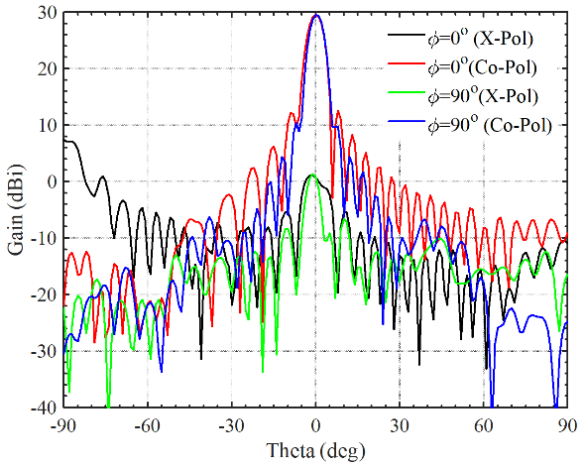


(a) at 28 GHz

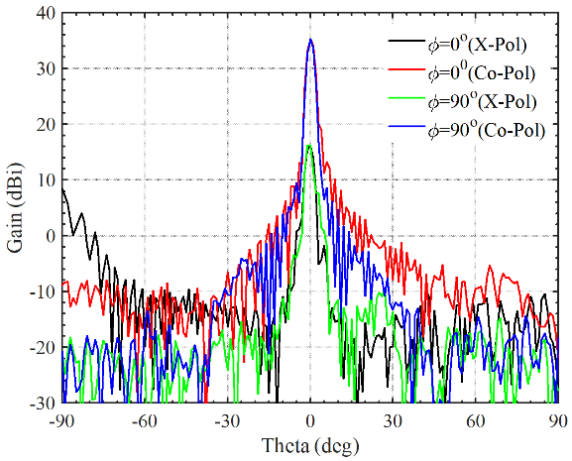


(b) at 60 GHz

**Figure 11.** Simulated RHCP radiations of the dual-band reflectarray at 28 and 60 GHz in (a) and (b), respectively.

The feed is a dual-band circular corrugated horn antenna inserted with a central dielectric tapered rod, as shown in Figure 10. This dielectric rod is made of polyphenylene ether (PPE) with a dielectric constant by 3, and may reduce the radius of the circular waveguide to assure a cutoff frequency below 60 GHz, which has linear and step tapers on the two sections inside the waveguide and horn, respectively for good impedance matching. The excitations to the horn by these two frequencies are performed by two orthogonal mode transformers (OMTs) integrated to form a coaxial connector. The radiation characteristics of feed antenna are summarized in Table 1 with detailed descriptions in Wang et al. (2018). The feed's radiation beamwidths are roughly 52°~57° at both frequencies to reduce truncation effects from the reflectarray. The axial ratios (ARs) are smaller than 0.16 dB. The frequency bandwidths of -10 dB reflection coefficients are more than 0.5 and 1 GHz, respectively (roughly 1.8 and 1.6%) for the 28 and 60 GHz bands, where the isolations are better than 60 and 80 dB. Even though the frequency bands are only roughly 2% due to the sophisticated metal structures to produce CP radiation, they have been successfully employed to exhibit the basic characteristics of the proposed dual-band reflectarray antennas without lossing the generality, as shown in the following discussion.

**Table 1** *Radiation Characteristics of the Dual-Band Corrugated Feed Horn (Wang et al., 2018)*

| Freq. | Gain | -10 dB Beamwidth | SLL | AR | |
|---|---|---|---|---|---|
| 28 GHz | 17 dBi | 56° | 52.2° | -35/-35 dB | 0.164 dB |
| 60 GHz | 17.1 dBi | 52° | 55° | -25.4/-32.3 dB | 0.043 dB |

To illuminate the reflectarray, the dual-band feed was placed at mm according to the illustration in Figure 6. The beam directions of the feed at these two frequency bands points to the same direction by 30.96$^{o}$ upward along the vertical plane to produce a specular direction for the directional beams. It is noted that the difference of phase center between these two bands is 0.58 mm, at 28 GHz, resulting in insignificant defocusing effects.

Figures 11a and 11b show the radiation patterns of right-hand circular polarization (RHCP) at 28 and 60 GHz, respectively. In this case, the z-axis of the radiations' coordinate system is set along the beam direction for easy exhibition. It is seen that the achieved gains are 29.56 and 35.38 dBi at 28 and 60 GHz, respectively, resulting in aperture efficiencies of 57% and 51%, respectively. The spillover efficiencies are 83%. In addition, the SLLs are -17 and -22 dB at 28 and 60 GHz, respectively. The axial ratios are 0.62 and 1.85 dB at 28 and 60 GHz, respectively. Finally, comparisons to similar dual-band metallic reflectarray antennas in Deng et al. (2017a), (2017b), and Zhao et al. (2017) are summarized in Table 2 as a reference of comparison. It is seen that the proposed reflectarray has similar aperture efficiencies and 1-dB gain variation bandwidths with a simplier architecture. However, at the LF band, the proposed reflectarray has a larger bandwidth of 13.21%.

**Table 2** *Comparison to the Similar Metal Reflectarray Works (Unit: GHz for Frequency, and % for Aperture Efficiency and 1-dB Gain Bandwidth)*

| Reference | Deng et al. (2017b) | Zhao et al. (2017) | Deng et al. (2017a) | Proposed (sim. |
|---|---|---|---|---|
| Frequency | 15/10 | 35/16 | 20/10 | 60/28 |
| Apert. Effic. Efficiency | 51.3/51.1 | - | 58/61 | 57/51 |
| 1-dB Gain Var. BW | 11.5/17.5 | (-3dB BW) 11.46/7.5 | 9.1/14 | 13.21 |

## 6 Conclusions

A metal reflectarray antenna is presented by using waveguide type elements to produce resonant and non-resonant modes for dual-band operation. Design rules are also shown for easy implementation. Examples have been demonstrated and cross-validated by full-wave numerical simulations of three major EM full-wave solvers of HFSS, FEKO and CST. Both linear and circular polarization radiations have been examined for this hybrid reflectarray architecture. This type of hybrid antenna elements has shown great potentials for reflectarray antennas with very high-power efficiency, whose applications will be explored in the future phases of studies.

**Acknowledgments**

This research was funded in parts by the Ministry of Science and Technology, Taiwan, National Taiwan University, Taiwan under projects 108L893702, Thailand Science Research and Innovation Fund, and King Mongkut's University of Technology North Bangkok with Contract no. KMUTNB-FF-65-21.

**References**


Almajali, E., McNamara, D. A., Shaker, J., & Chaharmir, M. R. (2014). Feed image lobes in offset-fed reflectarrays: Diagnosis and solution. *IEEE Transactions on Antennas and Propagation*, 62(1), 216-227. https://doi.org/10.1109/TAP.2013.2288977

An, W., Xu, S., & Yang, F. (2014). A metal-only reflectarray antenna using slot-type elements. *IEEE Antennas and Wireless Propagation Letters*, 13, 1553-1556. https://doi.org/10.1109/LAWP.2014.2342376

Ansys. (2013). *HFSS 14, Ansys.* Retrieved from: https://www.ansys.com/products/electronics/ansys-hfss

Balanis, C. A. (1997). *Antenna theory: Analysis and design.* Wiley.

Berry, D. G., Malech, R. G., & Kennedy, W. A. (1963). The reflectarray antenna. *IEEE Transactions on Antennas and Propagation*, 11(6), 645-651. https://doi.org/10.1109/TAP.1963.1138112

Bozzi, M., Germani, S., & Perregrini, L. (2004). A figure of merit for losses in printed reflectarray elements. *IEEE Antennas and Wireless Propagation Letters*, 3, 257-260. https://doi.org/10.1109/LAWP.2004.836577

Cho, Y. H., Byun, W. J., & Song, M. S. (2011). High gain metal-only reflectarray antenna composed of multiple rectangular grooves. *IEEE Transactions on Antennas and Propagation*, 59(12), 4559-4568. https://doi.org/10.1109/TAP.2011.2165479

Chou, H.-T., Lin C.-Y., & Wu, M.-H. (2015). A high efficient reflectarray antenna consisted of periodic all-metallic elements for the Ku-band DTV applications. *IEEE Antennas and Wireless Propagation Letters*, 14, 1542-1545. https://doi.org/10.1109/LAWP.2015.2411750

Chou, H.-T., Ho, H.-K., & Chen, Y.-J. (2016). Radiation discrepancy analysis for metallic reflectarray antennas with random manufacture distortion at mmW frequencies. *IEEE Antennas and Wireless Propagation Letters*, 15, 1885-1888. https://doi.org/10.1109/LAWP.2016.2542276

Chou, H.-T. & Liu, J. W.( 2018a). Synthesis and characteristic evaluation of convex metallic reflectarray antennas to radiate relatively orthogonal multi-beams. *IEEE Transactions on Antennas and Propagation*, 66(8), 4008-4016. https://doi.org/10.1109/TAP.2018.2841422

Chou, H.-T., Chen, Y.-J., & Ho, H.-K. (2018b). An all-metallic reflectarray and its element design: exploring the radiation characteristics of antennas for directional beam applications. *IEEE Antennas and Propagation Magazine*, 60(5), 41-51. https://doi.org/10.1109/MAP.2018.2859166

Chou, H.-T., Lertwiriyaprapa, T., Akkaraekthalin, P., & Torrungrueng, D. (2020). Flexible dual-band dual-beam radiation of reflector antennas by embedding resonant phase alignment elements for power refocusing.

*IEEE Transactions on Antennas and Propagation*, 68(6), 4259 - 4270. https://doi.org/10.1109/TAP.2020.2969711

Dassault Systèmes. (2012). *CST Studio Suite 2012*, *Dassault Systèmes*. Retrieved from: https://www.3ds.com/products-services/simulia/products/cst-studio-suite/solvers/

Deng, R., Yang, F., Xu, S., & Li, M. (2016). A 100-GHz metal-only reflectarray for high-gain antenna applications. *IEEE Antennas and Wireless Propagation Letters*, 15, 178-181. https://doi.org/10.1109/LAWP.2015.2436824

Deng, R., Yang, F., Xu, S., & Li, M. (2016). A low-cost metal-only reflectarray using modified slot-type phoenix element with 360° phase coverage. *IEEE Transactions on Antennas and Propagation*, 64(4), 1556-1560. https://doi.org/10.1109/TAP.2016.2526258

Deng, R., Xu, S., Yang, F., & Li, M. (2017). Single-layer dual-band reflectarray antennas with wide frequency ratios and high aperture efficiencies using phoenix elements. *IEEE Transactions on Antennas and Propagation*, 65(2), 612-622. https://doi.org/10.1109/TAP.2016.2639023

Deng, R., Xu, S., Yang, F., & Li, M. (2017). Design of a low-cost single-layer X/Ku dual-band metal-only reflectarray antenna. *IEEE Antennas and Wireless Propagation Letters*, 16, 2106-2109. https://doi.org/10.1109/LAWP.2017.2698099

Altair. (2011). *FEKO 6.1*, *Altair*. Retrieved from: https://www.altair.com/feko/

Lee, W., Yi, M., So, J., & Yoon, Y. J. (2015). Non-resonant conductor reflectarray element for linear reflection phase. *Electronics Letters*, 51(9), 669-671. https://doi.org/10.1049/el.2015.0194

Lee, W., & Yoon, Y. J. (2017). A broadband dual-metallic-reflectarray antenna for millimeter-wave applications. *IEEE Antennas and Wireless Propagation Letters*, 16, 856-859. https://doi.org/10.1109/LAWP.2016.2610002

Malfajani, R. S., & Atlasbaf, Z. (2014). Design and implementation of a dual-band single layer reflectarray in X and K bands. *IEEE Transactions on Antennas and Propagation*, 62(8), 4425-4431. https://doi.org/10.1109/TAP.2014.2327137

Pozar, D. M. (1998). *Microwave engineering*. Wiley.

Rahmat-Samii, Y., & Lee, S.-W. (1983). Directivity of planar array feeds for satellite reflector applications. *IEEE Transactions on Antennas and Propagation*, 31(3), 463–470. https://doi.org/10.1109/TAP.1983.1143061

Rajagopalan, H., & Rahmat-Samii, Y. (2008). Dielectric and conductor loss quantification for microstrip reflectarray: simulations and measurements. *IEEE Transactions on Antennas and Propagation,* 56(4), 1192-1196. https://doi.org/10.1109/TAP.2008.919225

Wang, N.-N., Wang, L.-Q., Fang, M., & Chou, H.-T. (2017). Design of dual-band metallic reflectarray antennas. In *2017 International Symposium on Antennas and Propagation (ISAP2017)* (pp. 1-2). https://doi.org/10.1109/ISANP.2017.8228766

Wang, N.-N., Zhao, B.-X., Fang, M., Qiu, J.-H., & Xiao, L.-Y. (2018). A high-gain dual-frequency dual-polarization feed system for 5G communication. In *2018 IEEE International Symposium on Antennas and Propagation & USNC/URSI National Radio Science Meeting* (pp. 1993-1994).

https://doi.org/10.1109/APUSNCURSINRSM.2018.8608472

Yi, M., Lee, W., & So, J. (2014). Design of cylindrically conformed metal reflectarray antennas for millimetre-wave applications. *Electronics Letters*, 50(20), 1409-1410. https://doi.org/10.1049/el.2014.2206

Zhao, J., Li, T., Cui, X., Zhao, X., Li, H., Hu, B., Wang, H., Zhou, Y., Liu, Q. (2017). A low-mutual coupling dual-band dual-reflectarray antenna with the potentiality of arbitrary polarizations. *IEEE Antennas and Wireless Propagation Letters*, 16, 3224-3227. https://doi.org/10.1109/LAWP.2017.2771205